JOURNAL OF COMPUTATIONAL PHYSICS 120, 128–144 (1995)

A Level Set Approach to a Unified Model for Etching, Deposition, and Lithography I: Algorithms and Two-Dimensional Simulations

D. ADALSTEINSSON AND J. A. SETHIAN*

Department of Mathematics and Lawrence Berkeley Laboratory, University of California, Berkeley, California 94720

Received September 27, 1994; revised February 2, 1995

We apply a level set formulation to the problem of surface advancement in a two-dimensional topography simulation of deposition, etching, and lithography processes in integrated circuit fabrication. The level set formulation is based on solving a Hamilton–Jacobi type equation for a propagating level set function, using techniques borrowed from hyperbolic conservation laws. Topological changes, corner and cusp development, and accurate determination of geometric properties such as curvature and normal direction are naturally obtained in this setting. The equations of motion of a unified model, including the effects of isotropic and unidirectional deposition and etching, visibility, surface diffusion, reflection, and material dependent etch/deposition rates are presented and adapted to a level set formulation. The development of this model and algorithm naturally extends to three dimensions in a straightforward manner and is described in part II of this paper (in press).

I. INTRODUCTION

In this paper, we develop a level set formulation to simulated deposition, etching, and lithography in integrated circuit fabrication. Our central concern is an accurate, stable, and efficient technique for surface advancement due to complex motion which, under different physical effects, may include effects of anisotropy, visibility conditions, and material-dependent propagation rates. In this paper, which focuses on a two-dimensional simulation, and the accompanying paper "A Level Set Approach to a Unified Model for Etching, Deposition, and Lithography II" which extends this work to three-dimensional topographic simulation, the validity of various physical models for the microfabrication project will not be examined. Instead, we hope to provide a robust numerical approach to these phenomena which can then be used to systematically examine various models.

A variety of numerical algorithms are available to advance fronts in etching, deposition, and lithography processes. These methods are not unique to such simulations and, in fact, are in use in such areas as dendritic growth and solidification, flame/combustion models, and fluid interfaces. Roughly speaking, they fall into three general categories:

- *Marker/string methods.* In these methods, a discrete parametrized version of the interface boundary is used. In two dimensions, marker particles are used; in three dimensions, a nodal triangularization of the interface is often developed. The positions of the nodes are then updated by determining front information about the normals and curvature from the marker representation. Such representations can be quite accurate; however, limitations exist for complex motions. To begin, if corners and cusps develop in the evolving front, markers usually form "swallowtail" solutions which must be removed through delooping techniques which attempt to enforce an entropy condition inherent in such motion (see [27]). Second, topological changes are difficult to handle; when regions merge, some markers must be removed. Third, significant instabilities in the front can result, since the underlying marker particle motions represent a weakly ill-posed initial value problem (see [20]). Finally, extensions of such methods to three dimensions require additional work.

- *Cell-based methods.* In these methods, the computational domain is divided into a set of cells which contain "volume fractions." These volume fractions are numbers between 0 and 1 and represent the fraction of each cell containing the physical material. At any time, the front can be reconstructed from these volume fractions. Advantages of such techniques include the ability to easily handle topological changes, adaptive mesh methods, and extensions to three dimensions. However, determination of geometric quantities such as normals and curvature can be inaccurate.

- *Characteristic methods.* In these methods, "ray-trace"-like techniques are used. The characteristic equations for the propagating interface are used, and the entropy condition at forming corners (see [27]) is formally enforced by constructing the envelope of the evolving characteristics. Such methods handle the looping problems more naturally, but they may be complex in three dimensions and require the adaptive addition and/or removal of rays, which can cause instabilities and/or over-smoothing.

* Supported in part by the Applied Mathematics Subprogram of the Office of Energy Research under Contract DE-AC03-76SF00098, and the National Science Foundation and DARPA Under Grant DMS-8919074.

0021-9991/95 $12.00

Level set methods, introduced in [20], offer a highly robust and accurate method for tracking interfaces moving under complex motions. Their major virtue is that they naturally construct the fundamental weak solution to surface propagation posed by Sethian [26, 27]. They work in any number of space dimensions, handle topological merging and breaking naturally, and are easy to program. They approximate the equations of motion for the underlying propagating surface, which resemble Hamilton–Jacobi equations with parabolic right-hand sides. The central mathematical idea is to view the moving front as a particular level set of a higher dimensional function. In this setting, sharp gradients and cusps are easily tracked, and the effects of curvature may be easily incorporated. The key numerical idea is to borrow the technology from the numerical solution of hyperbolic conservation laws and transfer these ideas to the Hamilton–Jacobi setting, which then guarantees that the correct entropy satisfying solution will be obtained.

In this paper, we apply these level set techniques to etching, deposition, and lithography problems in two space dimensions. The resulting numerical method allows one to accurately predict two-dimensional profile evolution, naturally taking into account such effects as incident angles, masks, yield functions, visibility, and anisotropy on the surface motion. Due to the use of conservative upwind schemes, the method selects the correct weak solution: where shocks in the tangent occur, the necessary entropy condition is invoked; at outward-facing corners the correct rarefaction fan solution is built. The method is second-order accurate in the motion of the front and is of the same computational work as cell and marker particle methods; that is, the work is a constant times the number of points which characterize the evolving front. The technique extends in a completely straightforward manner to three dimensions with minimal change to the algorithm; the three-dimensional version will be reported on elsewhere [2].

The outline of this paper is as follows. In Section I, we describe the basic level set algorithm applied to propagating interfaces. In Section II, we give a unified set of equations for the motion of an interface under deposition, etching, and lithography. In Section III, we give the reformulation of these equations in the level set perspective. In Section IV, we discuss some details of the numerical implementation. In Section V, we perform a series of numerical tests to verify the method, and in Section VI, we apply the method to three different problems. In Section VII, future work is discussed.

2. NUMERICAL ALGORITHMS FOR PROPAGATING FRONTS

2.1. Entropy Conditions and Curvature

The fundamental aspects of front propagation in our context can be illustrated as follows. Let $\gamma(0)$ be a smooth, closed initial curve in R^2, and let $\gamma(t)$ be the one-parameter family of curves generated by moving $\gamma(0)$ along its normal vector field with speed $F(K)$. Here, $F(K)$ is a given scalar function of the curvature K. Thus, $n \cdot x_t = F(K)$, where $x(s, t)$ is the position vector parameterized by s at time t, and n is the unit normal to the curve.

Consider a speed function of the form $1 - \varepsilon K$, where ε is a constant. An evolution equation for the curvature K (see [27]) is given by

$$K_t = \varepsilon K_{\alpha\alpha} + \varepsilon K^3 - K^2, \tag{1}$$

where we have taken the second derivative of the curvature K with respect to arclength α. This is a reaction–diffusion equation; the drive toward singularities due to the reaction term $(\varepsilon K^3 - K^2)$ is balanced by the smoothing effect of the diffusion term $(\varepsilon K_{\alpha\alpha})$. Indeed, with $\varepsilon = 0$, we have a pure reaction equation $K_t = -K^2$. In this case, the solution is $K(s, t) = K(s, 0)/(1 + tK(s, 0))$, which is singular in finite t if the initial curvature is anywhere negative. Thus, corners can form in the moving curve when $\varepsilon = 0$.

As an example, consider the periodic initial cosine curve

$$\gamma(0) = (-s, [1 + \cos 2\pi s]/2) \tag{2}$$

propagating with speed $F(K) = 1 - \varepsilon K$, $\varepsilon > 0$. As the front moves, the troughs at $s = n + \frac{1}{2}$, $n = 0, \pm 1, \pm 2, \ldots$ are sharpened by the negative reaction term (because $K < 0$ at such points) and smoothed by the positive diffusion term (see Fig. 1a). For $\varepsilon > 0$, it can be shown (see [27, 20]) that the moving front stays C^∞.

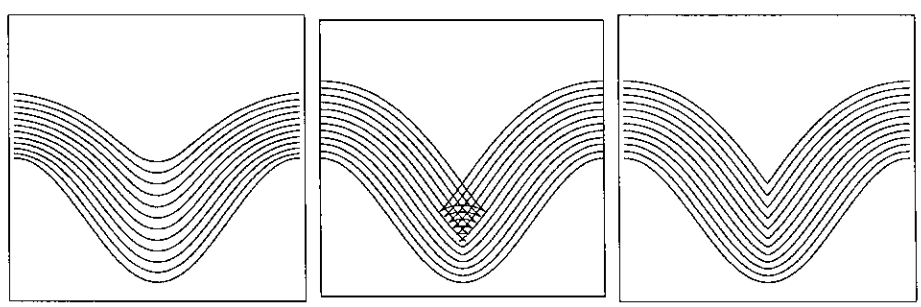

$F = 1. - 0.25K$ *Fig.1a.* | *Swallowtail*$(F = 1.0)$ *Fig.1b* | *Entropy Satisfying*$(F = 1.0)$ *Fig.1c*

FIG. 1. Propagating cosine curve.

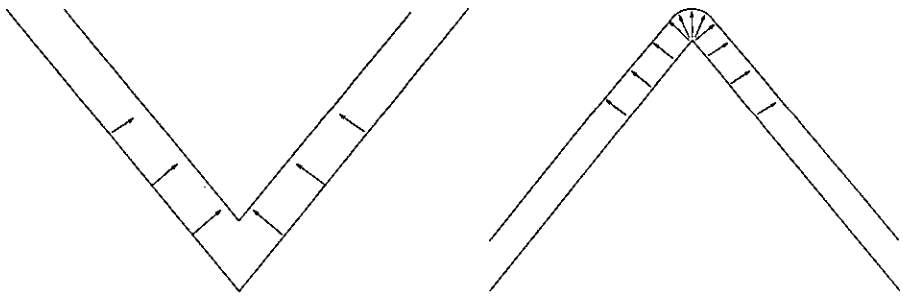

FIG. 2. Front propagating with unit normal speed.

On the other hand, for $\varepsilon = 0$, the front develops a sharp corner in finite time as discussed above. In general, it is not clear how to construct the normal at the corner and continue the evolution, since the derivative is not defined there. One possibility is the "swallowtail" solution formed by letting the front pass through itself (see Fig. 1b). However, from a geometrical argument it seems clear that the front at time t should consist of only the set of all points located a distance t from the initial curve. (This is known as the Huygens principle construction, see [27]). Roughly speaking, we want to remove the "tail" from the "swallowtail." In Fig. 1c, we show this alternate weak solution. Another way to characterize this weak solution is through the following "entropy condition" posed by Sethian (see [27]): If the front is viewed as a burning flame, then *once a particle is burnt it stays burnt.* Careful adherence to this stipulation produces the Huygens principle construction. Furthermore, this physically reasonable weak solution is the formal limit of the smooth solutions $\varepsilon > 0$ as the curvature term vanishes (see [27]).

As further illustration, we consider the case of a V-shaped front propagating normal to itself with unit speed ($F = 1$). In [26], the link between this motion and hyperbolic conservation laws is explained. In Fig. 2a, the point of the front is downwards; as it moves inwards with unit speed, a shock develops as the front pinches off, and an entropy condition is required to select the correct solution to stop the solution from being double-valued and to produce the limit of the viscous case. Conversely, in Fig. 2b, the corner in the front is upwards; in this case the unit normal speed results in a rarefaction fan which connects the left state with slope $+1$ to the right state which has slope -1. Extensive discussion of the role of shocks and rarefactions in propagating fronts may be found in [26].

The key to constructing numerical schemes which adhere to both this entropy condition and rarefaction structure comes from the link between propagating fronts and hyperbolic conservation laws. Consider the initial front given by the graph of $f(x)$, with f and f' periodic on [0, 1], and suppose that the propagating front remains a function for all time. Let ϕ be the height of the propagating function at time t, thus $\phi(x, 0) = f(x)$. The normal at (x, ϕ) is $(\phi_x, -1)$, and the equation of motion becomes $\phi_t = F(K)(1 + \phi_x^2)^{1/2}$. Using the speed function $F(K) = 1 - \varepsilon K$ and the formula $K = -\phi_{xx}/(1 + \phi_x^2)^{3/2}$, we get

$$\phi_t - (1 + \phi_x^2)^{1/2} = \varepsilon \frac{\phi_{xx}}{1 + \phi_x^2} \tag{3}$$

Differentiating both sides of this equation yields an evolution equation for the slope $u = d\phi/dx$ of the propagating front, namely

$$u_t + [-(1 + u^2)^{1/2}]_x = \varepsilon \left[\frac{u_x}{1 + u^2} \right]_x. \tag{4}$$

Thus, the derivative of the Hamilton–Jacobi equation with parabolic right-hand side for the changing height ϕ is a viscous hyperbolic conservation law for the propagating slope u (see [29]). The entropy condition in [27] is in fact equivalent to the one for propagating shocks in hyperbolic conservation laws. Thus, we exploit the numerical technology from hyperbolic conservation laws to build consistent, upwind schemes which select the correct entropy conditions. For details, see [20, 28].

Our goal then is to develop a front propagation scheme built on these curvature/viscosity ideas. Before doing so, we must extend the above ideas to include propagating fronts which are not easily written as functions. This is the level set idea introduced by Osher and Sethian [20].

2.2. Level Set Methods

Given a moving closed hypersurface $\Gamma(t)$, that is, $\Gamma : [0, \infty) \rightarrow R^N$, we wish to produce an Eulerian formulation for the motion of the hypersurface propagating along its normal direction with speed F, where F can be a function of various arguments, including the curvature, normal direction, etc. The main idea is to embed this propagating interface as the zero level set of a higher dimensional function ϕ. Let $\phi(x, t = 0)$, where $x \in R^N$ is defined by

$$\phi(x, t = 0) = \pm d, \tag{5}$$

where d is the distance from x to $\Gamma(t = 0)$, and the plus (minus) sign is chosen if the point x is outside (inside) the initial hypersurface $\Gamma(t = 0)$. Thus, we have an initial function $\phi(x, t = 0): R^N \rightarrow R$ with the property that

$$\Gamma(t = 0) = (x | \phi(x, t = 0). \tag{6}$$

Our goal is to now produce an equation for the evolving function $\phi(x, t)$ which contains the embedded motion of $\Gamma(t)$ as the level set $\phi = 0$. Let $x(t)$, $t \in [0, \infty)$ be the path of a point on the propagating front. That is, $x(t = 0)$ is a point on the initial front $\Gamma(t = 0)$ and $x_t \cdot n = F(x(H)$. Since the evolving function ϕ is always zero on the propagating hypersurface, we must have

$$\phi(x(t), t) = 0. \tag{7}$$

By the chain rule,

$$\phi_t + \nabla\phi(x(t), t) \cdot x'(t) = 0. \tag{8}$$

Since F already gives the speed in the outward normal direction, then $x'(t) \cdot n = F$ where $n = \nabla\phi/|\nabla\phi|$. Thus, we then have the evolution equation for ϕ, namely

$$\phi_t + F|\nabla\phi| = 0 \tag{9}$$

$$\phi(x, t = 0) \quad \text{given.} \tag{10}$$

We refer to this as a Hamilton–Jacobi "type" equation because, for certain forms of the speed function F, we obtain the standard Hamilton–Jacobi equation.

In Fig. 3 (taken from [30]) we show the outward propagation of an initial curve and the accompanying motion of the level set function ϕ. In Fig. 3a we show the initial circle, and in Fig. 3b we show the circle at a later time. In Fig. 3c we show the initial position of the level set function ϕ, and in Figure 3d we show this function at a later time.

There are four major advantages to this Eulerian Hamilton–Jacobi formulation. The first is that the evolving function $\phi(x, t)$ always remains a function as long as F is smooth. However, the level surface $\phi = 0$, and hence the propagating hypersurface $\Gamma(t)$, may change topology, break, merge, and form sharp corners as the function ϕ evolves (see [20]).

The second major advantage of this Eulerian formulation concerns numerical approximation. Because $\phi(x, t)$ remains a function as it evolves, we may use a discrete grid in the domain of x and substitute finite difference approximations for the spatial and temporal derivatives. For example, using a uniform mesh of spacing h, with grid nodes (i, j), and employing the standard notation that ϕ_{ij}^n is the approximation to the solution $\phi(ih, jh, n\Delta t)$, where Δt is the time step, we might write

$$\frac{\phi_{ij}^{n+1} - \phi_{ij}^n}{\Delta t} + (F)(\nabla_{ij}\phi_{ij}^n) = 0. \tag{11}$$

Here, we have used forward differences in time, and let $\nabla_{ij}\phi_{ij}^n$ represent some appropriate finite difference operator for the spatial derivative. As discussed above, the correct entropy-satisfying approximation to the difference operator comes from exploiting the technology of hyperbolic conservation laws. Following [20], given a speed function $F(K)$, we update the front

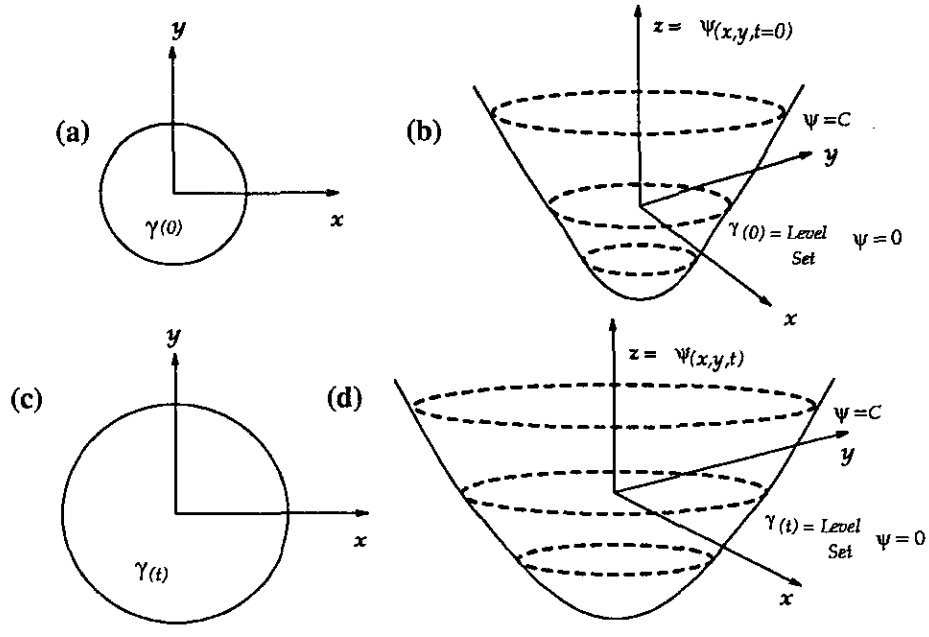

FIG. 3. Propagating circle.

by the following scheme. First, separate $F(K)$ into a constant advection term F_0 and the remainder $F_1(K)$, that is,

$$F(K) = F_0 + F_1(K). \tag{12}$$

The advection component F_0 of the speed function is then approximated using upwind schemes, while the remainder is approximated using central differences. In one space dimension with positive F_0, we have

$$\phi_i^{n+1} = \phi_i^n - \Delta t F_0[(\max(D_i^-, 0)^2 + \min(D_{i,0}^+)^2)^{1/2} - |F_1(K)\nabla\phi_i^n|]. \tag{13}$$

Extension to higher dimensions are straightforward; we use the version introduced in [33].

The third major advantage of the above formulation is that intrinsic geometric properties of the front may be easily determined from the level function ϕ. For example, at any point of the front, the normal vector is given by

$$\mathbf{n} = \frac{\nabla\phi}{|\nabla\phi|}, \tag{14}$$

and the curvature is easily obtained from the divergence of the gradient of the unit normal vector to front, i.e.,

$$K = \nabla \cdot \frac{\nabla\phi}{|\nabla\phi|} = -\frac{\phi_{xx}\phi_y^2 - 2\phi_x\phi_y\phi_{xy} + \phi_{yy}\phi_x^2}{(\phi_x^2 + \phi_y^2)^{3/2}}. \tag{15}$$

Finally, the fourth major advantage of the above level set approach is that there are no significant differences in following fronts in three space dimensions. By simply extending the array structures and gradients operators, propagating surfaces are easily handled.

As an example of the application of level set methods, consider once again the problem of a front propagating with speed $F(K) = 1 - \varepsilon K$. In Fig. 4, we show two cases of a propagating initial triple sin curve. For ε small (Fig. 4a), the troughs sharpen up and will result in transverse lines that come too close together. For ε large (Fig. 4b), parts of the boundary with high values of positive curvature can initially move inwards, and concave parts of the front can move quickly up.

Since its introduction in [20], the above level set approach has been used in a wide collection of problems involving moving interfaces. Some of these applications include the generation of minimal surfaces [6], singularities and geodesics in moving curves and surfaces in [7], flame propagation [23, 38], fluid interfaces [3, 5, 19], and shape reconstruction [16]. Extensions of the basic technique include fast methods in [1], level set techniques for multiple fluid interfaces and triple point junctions in [32], and grid generation in [30, 31]. The fundamental Eulerian perspective presented by this approach has since been adopted in many theoretical analyses of mean curvature flow, in particular, see [8, 4].

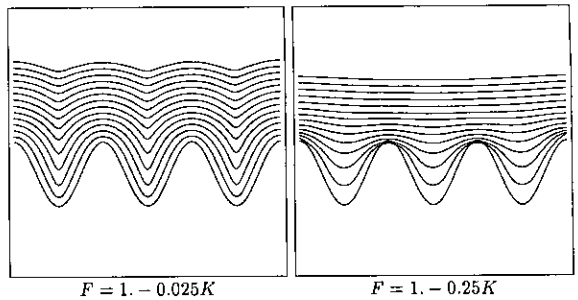

$F = 1. - 0.025K$ *Fig.4a.* $F = 1. - 0.25K$ *Fig.4b*

FIG. 4. Propagating triple sine curve.

3. EQUATIONS OF MOTION FOR DEPOSITION, ETCHING, AND LITHOGRAPHY

Our goal is now to build the speed function F for deposition, etching, and lithography in the level set equation of motion

$$\phi_t + F|\nabla\phi| = 0 \tag{16}$$

$$\phi(x, t = 0) \quad \text{given.} \tag{17}$$

Note that F is the speed in the normal direction. Our approach is to write the normal speed function as the superposition of the three main physical effects:

$$F = F_{\text{Deposition}} + F_{\text{Etching}} + F_{\text{Lithography}}. \tag{18}$$

Of course, all effect do not take place at once; however, the design of the numerical algorithm allows various combinations of terms to be "turned on" during any time step of the surface advancement.

The underlying physical effects involved in etching, deposition, and lithography are quite complex; much of the following summary is obtained from the excellent overviews in [24, 25, 35, 36, 17, 22]. The effects may be summarized briefly as follows:

• *Deposition.* Particles are deposited on the surface, which causes build-up in the profile. The particles may either isotropically condense from the surroundings (known as chemical or "wet" deposition), or be deposited from a source. In the latter case, we envision particles leaving the source and depositing on the surface; the main advantage of this approach is increased control over the directionality of surface deposition. The rate of deposition, and hence growth of the layer, may depend on source masking, visibility effects between the source and surface point, angle-dependent flux distribution of source particles, and angle of incidence of the particles relative to the surface

normal direction, reflection of deposited particles, and surface diffusion effects.

• *Etching.* Particles remove material from the evolving profile boundary. The material may be isotropically removed, known again as chemical or "wet" etching, or chipped away through reactive ion etching, also known as "ion milling." Similar to deposition, the main advantage of reactive ion etching is enhanced directionality, which becomes increasingly important as device sizes decrease substantially and etching must proceed in vertical directions without affecting adjacent features. As described in [34], the total etch rate consists of an ion-assisted rate and a purely chemical etch rate due to etching by neutral radicals, which may still have a directional component. As in the above, the total etch rate due to wet and directional milling effects can depend on source masking, visibility effects between the source and surface point, angle-dependent flux distribution of source particles, the angle of incidence of the particles relative to the surface normal direction, reflection/re-emission of etching/milling particles, and surface diffusion effects.

• *Lithography.* The underlying material is treated by an electromagnetic wave which alters the resist property of the material. The aerial image is found, which then determines the amount of crosslinking at each point in the material which then produces the etch/resist rate at each point of the material. A profile is then etched into the material, where the speed of the profile in its normal direction at any point is given by the underlying etch rate. The key factors that determine the evolving shape are the etch/resist profile and masking effects.

In the rest of this section, we formalize the above.

3.1. Initial Position and Setup

We consider a periodic initial curve $\gamma(s)$, $0 \le s \le 1$, where $x(s)$ is a point in R^2 on $\gamma(s)$. We also consider a source Z given as a curve above the initial curve, and write $Z(x)$ referring to the height of the source at the point x.

For both etching and deposition, define the source ray to be the ray leaving the source and aimed towards the surface profile. Let ψ be the angle variation in the source ray away from the y axis; ψ positive will correspond to an angle clockwise from the positive y axis. Let n be the normal vector at a point x on the surface profile, and θ the angle between the normal and the source ray.

In Fig. 5, we indicate these variables. Masks, which force flux rates to be zero, are indicated by heavy dark lines on the initial profile. The visibility angle Y is indicated by the region between the heavy dashed lines. Our goal is to write the effects of deposition, etching, and lithography on the speed F at a point x on the front $\gamma(s, t)$ obtained by updating the initial curve.

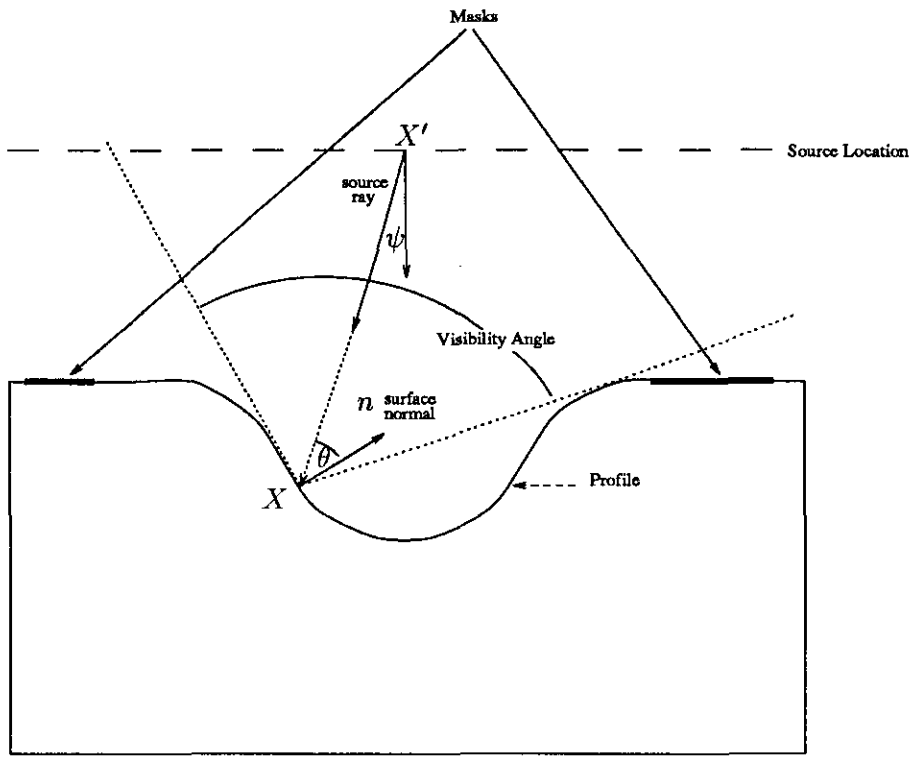

FIG. 5. Variables and setup.

3.2. Deposition

We consider three separate types of deposition:

- F^D_{Iso} (Isotropic deposition). Uniform deposition.
- F^D_{Uni} (Unidirection deposition). Deposition in a particular direction, based on the angle of the incoming stream.
- F^D_{Sou} (Source deposition). Deposition radiating from a point source.

In Fig. 5, we generalize all of these effects as the "source." Thus, the line source as shown in the figure may consist of locations which emit either unidirectional deposition or point source deposition.

The above terms may assembled as

$$F_{\text{Deposition}} = F_{\text{Deposition}}(F^D_{\text{Iso}}, F^D_{\text{Uni}}, F^D_{\text{Sou}}); \tag{19}$$

that is, the deposition speed may depend on isotropic, unidirectional, or source deposition.

Let us now change notation and let $M_{Y(x,x')}$ be one if the point x' on the source is visible from the point x on the profile, and zero otherwise. Let r be the distance from x to x', and, finally, let α be the unit vector at the point x' on the source pointing towards the point x on the profile. Then we may refine the above terms as:

3.2.1. *Isotropic Deposition*

$$F^D_{\text{Iso}} = R^D_{\text{Iso}}\text{Flux}^D_{\text{Iso}}. \tag{20}$$

Here, R^D_{Iso}, is the rate of growth and $\text{Flux}^D_{\text{Iso}}(x)$ is the isotropic flux function.

3.2.2. *Unidirectional Deposition*

$$F^D_{\text{Uni}} = R^D_{\text{Uni}}(x)M_{Y(x,x')}\text{Flux}^D_{\text{Uni}}(r, \psi, \theta, x)(\mathbf{n} \cdot \boldsymbol{\alpha}). \tag{21}$$

Here, R^D_{Uni} is the rate of growth, and $\text{Flux}^D_{\text{Uni}}(r, \psi, \theta, x)$ is the unidirectional flux function, which may depend on the distance r from x to the source, the emission angle ψ, the angle of incidence θ, and the starting point x'.

3.2.3. *Source Deposition*

$$F^D_{\text{Sou}} = R^D_{\text{Sou}}(x)\int_{-\pi/2}^{\pi/2} \text{Flux}^D_{\text{Sou}}(r, \psi, \theta, x)M_{Y(x,x')}(\mathbf{n} \cdot \boldsymbol{\alpha})\, d\sigma. \tag{22}$$

Here, the integral is over all angles σ between $-\pi/2$ and $\pi/2$, R^D_{Sou} is the rate of growth, and $\text{Flux}^D_{\text{Sou}}(r, \psi, \theta, x)$ is the flux function. A typical flux function might include the effects of sputter deposition and be of the form $\cos^n(A\psi)$, where n is a constant and $|\psi| \leq 2\pi A$.

3.3. Etching

In this formulation, the equations of etching are quite similar; we include them for the sake of completeness. We consider three separate types of etching:

- F^E_{Iso} (Isotropic etching). Uniform etching. This may be a function of the underlying material.
- F^E_{Uni} (Unidirection etching). Etching in a particular direction, based on the angle of the incoming stream.
- F^E_{Sou} (Source etching). Etching radiating from a point source, including ion-milling and transport of neutral radicals.

The above terms may assembled as

$$F_{\text{Etching}} = F_{\text{Etching}}(F^E_{\text{Iso}}, F^E_{\text{Uni}}, F^E_{\text{Sou}}), \tag{23}$$

where again we may refine the above terms as:

3.3.1. *Isotropic Etching*

$$F^E_{\text{Iso}} = R^E_{\text{Iso}}\text{Flux}^E_{\text{Iso}}. \tag{24}$$

Here, R^E_{Iso} is the etch rate based on the isotropic flux function $\text{Flux}^E_{\text{Iso}}(r)$.

3.3.2. *Unidirectional Etching*

$$F^E_{\text{Uni}} = R^E_{\text{Uni}}(x)M_{Y(x,x')}\text{Flux}^E_{\text{Uni}}(r, \psi, \theta, x)(\mathbf{n} \cdot \boldsymbol{\alpha}). \tag{25}$$

Here, R^E_{Uni} is the etch rate, and $\text{Flux}^E_{\text{Uni}}(r, \psi, \theta, x)$ is the unidirectional flux function, which may depend on the distance r from x to the source, the emission angle ψ, the angle of incidence θ, and the starting point x. A typical flux function might be of the form $\cos^n(A\psi)$, where n is a constant and $|\psi| \leq 2\pi A$.

3.3.3. *Source Etching*

$$F^E_{\text{Sou}} = R^E_{\text{Sou}}(x)\int_{-\pi/2}^{\pi/2} \text{Flux}^E_{\text{Sou}}(r, \psi, \theta)M_{Y(x,x')}(\mathbf{n} \cdot \boldsymbol{\alpha})\, d\sigma. \tag{26}$$

Here, the integral is over all angles σ between $-\pi/2$ and $\pi/2$, R^E_{Sou} is the rate of growth, and $\text{Flux}^E_{\text{Sou}}(r, \psi, \theta, x)$ is the flux function.

3.4. Lithography

The construction of the speed function for lithographic cases is extremely straightforward if one assumes that the etch rate is given. Typically, an aerial image is found using a simulator such as SPLAT [37], which, together with a program such as BLEACH [37], provides the etch rate at each point of the material. Since the etch rate is provided everywhere in the material, we may simply write

$$F_{\text{Lithography}} = R_{\text{Litho}}, \tag{27}$$

where the etch rate R_{Litho} is supplied by the simulator.

3.5. Other Effects

In etching and deposition, additional effects can play an important role in the evolving profile. These include:

• *Surface migration.* Migration of particles as they collide with the interface. This causes a diffusion-like term which tends to diffuse large deposition peaks. Given the above speed function F for surface motion, one can think of two ways to include the effects of surface diffusion/migration. One is to simply modify the speed function by the term $1 - \varepsilon K$, where K is the local curvature. As discussed in Section II, this has the effect of diffusing the front. The second way is to obtain a more accurate representation of the diffusion term as follows. Given a curve $x(s)$ in R^2, we imagine that a scalar function $g(s)$ is defined on that curve. We want to solve the diffusion equation $g_t = \varepsilon g_{ss}$, where s is differentiation with respect to arc-length. Clearly, the limit as time approaches infinity is a constant value of g along the curve $x(s)$. Thus, we can modify the speed function F by solving the above diffusion equation on the front.

• *Re-emission/reflection.* Some of incoming flux/neutral radicals may not stick to the surface, but instead be reflected/re-emitted. The fraction of particles that are not reflected/re-emitted is known as the "sticking probability" and varies between 0 and 1. Thus, a sticking probability of unity corresponds to the case under study above. For sticking probabilities less than unity, and depending on the surface physics, the re-emission can be either specular or diffusive. Thus, each point on the evolving profile may act as additional source when viewed from other visible sites on the front. This can be set up as an integral equation for the total source flux at a point, depending on the seen visible angle and probability flux re-emission distribution. For details see the derivation in [34] and the calculations in [18]. This integral yields a dense, non-symmetric matrix which needs to be solved at every time step in order to calculate the correct flux to advance the front. In two dimensions this is tractable; in three dimensions the problem is daunting and requires significant resources.

4. FUNDAMENTAL IDEAS OF IMPLEMENTATION

Here, we discuss the numerical implementation of the above equations of motion in the level set formulation given by Eq. (16), using the version of the numerical approximation of Eq. (13) given in [33]. For details we refer the reader to [28].

4.1. The Narrow-Band Formulation

The main issue in the level set approach is the extension of the speed function F given by Eq. (18) to all of space in order to move all the level sets, not simply the zero level set on which the speed function is naturally defined. While this may be straightforward in some cases (such as in lithography, see below), it is not efficient, since one must perform considerable computational labor away from the front to advance the other level sets.

Consequently, we adopt the approach introduced in [6], used in recovering images in [16], and analyzed extensively in [1], and focus our computational effort in a narrow band about the zero level set. We only update the values of the level set function ϕ in this thin zone around the interface. Thus, in two dimensions, an $O(N^2)$ calculation, where N is the number of grid points per side, reduces to an $O(kN)$ calculation, where k is the number of cells in the narrow band. Typically, this is considerably faster than marker particle methods, due to the need for many marker points per mesh cell in order to obtain acceptable accuracy. As the front moves, the narrow band must occasionally be rebuilt (known as "re-initialization") of the interface. For details see [6, 16, 1].

Briefly, the entire two-dimensional grid of data is stored in a square array. A one-dimensional object is used to keep track of which points in this array correspond to the tube, and the values of ϕ at those points are updated. When the front moves half the distance towards the edge of the tube boundary, the calculation is stopped, and a new tube is built with the zero level set interface boundary at the center. Details on the accuracy, typical tube sizes, and number of times a tube must be rebuilt may be found in [1].

4.2. Lithography

The application of the level set approach to lithography is straightforward, since the etch/resist rate at each grid point is supplied as input. Some calculations of lithographic problems exploiting the level set/conservation law of [20] were made by Helmsen (see [11, 10]) studying various etch functions from different aerial images, including thin film effects.

In the case of lithography, as mentioned above, we use a narrow band approach, as well as a second-order in space conservative advancement scheme as outlined in [20], modified as in [33]. This yields a method which is both considerably faster than the full matrix approach and less diffusive than the first-order scheme used in [10]; the difference between the two methods is discussed in detail in the results section.

4.3. Etching and Deposition

To advance the front according to etching/deposition, we distinguish between local variables, which are easily calculated at each grid point within the narrow band, and front-based extension variables, which are most naturally defined only at the moving interface. The general philosophy is to use values of local variables wherever they can be calculated, and extension variables from the front to the grid points in the narrow band only when necessary. Once all the variables are assembled at each grid point (those obtained from local calculations and those obtained by extensions), the speed function in Eq. (18) is then evaluated.

Local variables such as surface normals and curvature are

easily calculated from the grid information as discussed extensively in [33]. The main idea is to construct at each grid point the local variables for the level set passing through that grid point. Thus, if at grid point (i, j) the value of ϕ is ϕ_0, then we find the normal vector and curvature of the level surface passing through that grid point whose level value is ϕ_0. The values of ϕ at each grid point will then be updated by evaluating the speed function at the grid using the values of the local variables; this results in an approximation of the updated position of the zero level set corresponding to the real front.

Variations in etch rate as a function of material properties are local variables, and are easily handled by marking the given material properties at each grid point within the tube. Wide variations in the etch rate are easily handled.

The main front-based extension variable that must be determined is the visibility at a given point x of the interface. That is, we must construct values for the visibility function at each grid point, even though it only has real meaning for points on the zero level set corresponding to the interface. This is done as follows. At each grid point above the interface we compute the seen angle relative to the zero level set, and use this value of the visibility term at that point. At each point below the interface, previous values are used to determine the appropriate speed; those values are directly employed as the visibility values for the new position. This technique yields the visibility angles at each grid point in the narrow tube, which is then used to evaluate the full speed function in Eq. (18).

Variations in etch rate as a function of material properties are easily handled by marking the given material properties at each grid point within the tube. Of course, wide variations in the etch rate are easily handled.

Masks are handled by requiring that no motion be executed below a mask; this is accomplished by creating a new tube matrix whenever updated which is reset to old values at grid points that are masked.

4.4. Updating the Front

We update the front using a second order in space scheme as described in [20, 28]. In the one-dimensional case, the first-order scheme in the case of speed $F = 1$ is given by

$$\phi_i^{n+1} = \phi_i^n - \Delta t[(\max(D_i^-, 0)^2 + \min(D_i^+, 0)^2)^{1/2}]. \quad (28)$$

A second-order version is provided by

$$\phi_i^{n+1} = \phi_i^n - \Delta t[(\max(A, 0)^2 + \min(B, 0)^2)^{1/2}], \quad (29)$$

where

$$A = D_i^- + \frac{\Delta x}{2} m(D_i^{--}, D_i^{+-}) \quad (30)$$

$$B = D_i^+ - \frac{\Delta x}{2} m(D_i^{++}, D_i^{+-}), \quad (31)$$

where D^{--}, D^{-+}, and D^{++} are backwards, centered, and forward second-order difference operators, and the switch function m is given by

$$m(x, y) = \begin{cases} x & \text{if } |x| \le |y| \\ y & \text{if } |x| > |y| \end{cases} \quad \text{if } xy \ge 0$$
$$\{0 \qquad\qquad\} \quad \text{if } xy < 0. \quad (32)$$

The construction of the two-dimensional version of this scheme, using operator splitting is straightforward. We have

$$\phi_{ij}^{n+1} = \phi_{ij}^n - \Delta t[(\max(A, 0)^2 + \min(B, 0)^2 + \max(C, 0)^2 + \min(D, 0)^2)^{1/2}], \quad (33)$$

where

$$A = D_{ij}^{-x} + \frac{\Delta x}{2} m(D_{ij}^{-x-x}, D_{ij}^{+x-x}) \quad (34)$$

$$B = D_{ij}^{+x} - \frac{\Delta x}{2} m(D_{ij}^{+x+x}, D_{ij}^{+x-x}) \quad (35)$$

$$C = D_{ij}^{-y} + \frac{\Delta y}{2} m(D_{ij}^{-y-y}, D_{ij}^{+y-y}) \quad (36)$$

$$D = D_{ij}^{+y} - \frac{\Delta y}{2} m(D_i^{+y+y}, D_{ij}^{+y-y}), \quad (37)$$

where D^{-x-x}, D^{-x+x}, and D^{+x+x} are backwards, centered, and forward second-order difference operators in x; similar expressions hold in the y direction. The switch function m is defined the same as above. Extension to three dimensions is straightforward and discussed in detail in [2].

5. NUMERICAL TESTS OF METHOD

In this section, we perform numerical tests to verify the accuracy and efficiency of the method.

5.1. Deposition

5.1.1. *Source Deposition*

We begin by studying source deposition into a trench. In Fig. 6 we take a deposition source above a trench, where deposition material is emitted from a line source from the solid line above the trench. In this experiment, the deposition rate is the same in all directions. The effects of shadowing are considered. In Fig. 6a, we show results for 40 computational cells along the width of the compute region (between the two vertical dashed lines, Fig. 6b has 80 cells, and Fig. 6c has 160 cells. The time step for all three calculations is $\Delta t = 0.00625$. The calculations are performed with a narrow band tube width of six cells on either side of the front. There is little change between the

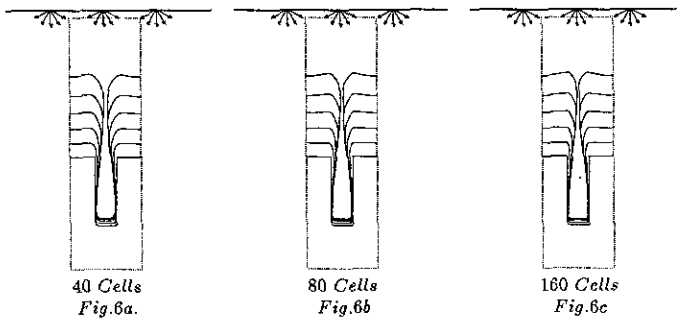

FIG. 6. Source deposition into trench.

calculation with 80 cells and the one with 160 cells, indicating that the solution is converged.

As the walls pinch toward each other, the seen visible angle decreases and the speed diminishes.

Next, in Fig. 7, we study a deposition problem in which a cavity on the right is hidden from the deposition source. This cavity grows very slowly, and material fills above it until it is shut off. The calculation is presented on a grid with 160 cells in the horizontal direction and again a tube width of six cells on each side of the interface.

5.1.2. *Directional Deposition*

Next, we consider directional deposition. Material emits from the line source at an angle of 30° from the vertical. In Fig. 8, we show results at various times, starting with the initial state. Due to the effects of shadowing, the profile develops bumps as it evolves.

5.1.3. *Wet/Chemical Deposition*

Finally, for completeness we consider the case of wet/chemical deposition applied to the above cavity, in Fig. 9, we advance the profile in its normal direction at unit speed.

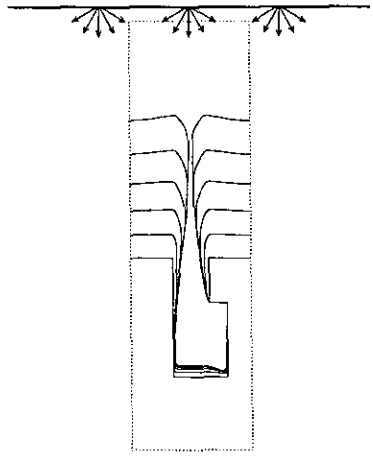

FIG. 7. Source deposition into cavity.

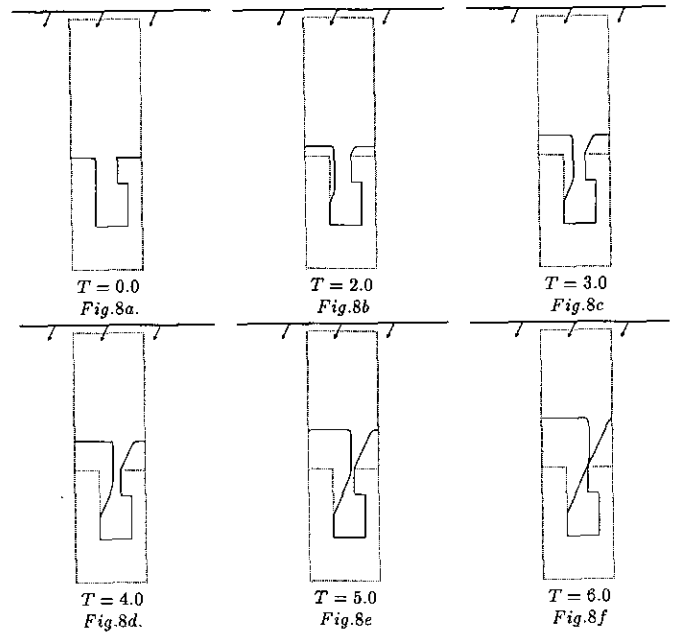

FIG. 8. Directional deposition into cavity.

5.2. Etching

5.2.1. *Source Etching*

We begin by considering source etching into a trench. The dark line again acts as a line source of etching material, evenly distributed in all angles. Visibility effects are considered. In Fig. 10a, we show the results with 40 horizontal cells; Fig. 10b has 80 cells and Fig. 10c has 160 cells. There is little difference between the last two figures, indicating that the results are converged. In this example there is no yield variation in the etch rate as a function of angle of incidence, thus corners immediately smooth out, since the correct rarefaction fan is built into this case (see [27]).

Next, in Fig. 11, we study the etching problem in which a cavity on the right is hidden from the etching source. The lip

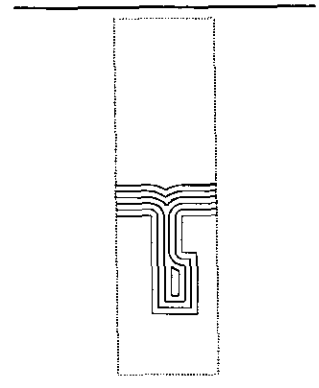

FIG. 9. Chemical deposition into cavity.

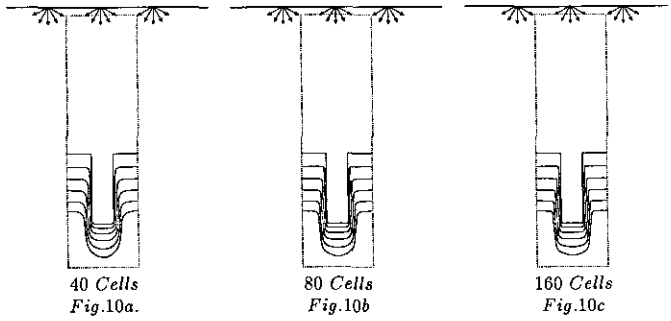

FIG. 10. Source etching into trench.

of the cavity is etched away until it breaks through, revealing the full expanse of the region. Source integration is over the source length and includes distance dependence.

5.2.2. *Directional Etching*

Next, we consider directional etching. Material emits from the line source at an angle of 30° from the vertical. In Fig. 12, we show results at various times, starting with the initial state. Again there is no yield variation in the etch rate due to angle of incidence with the normal; in other words, the speed of the profile in the normal direction is just the projection of the directional etch rate in that normal direction. Due to the effects of shadowing, as the profile evolves we again see that part of the profile aligns itself tangential to the incoming unidirectional etching stream.

5.2.3. *Wet/Chemical Etching*

Finally, for completeness we consider the case of wet/chemical etching applied to the above cavity. In Fig. 13, we advance the profile in its normal direction into the material at unit speed. One could choose to stop all motion inside a void once it forms on the basis of visibility, or continue the motion. In the figures we continued the motion; the other case is easily handled by a test of the connectedness of a contour.

5.3. Lithography

We begin by using a model Gaussian etch rate function. In a region which is one unit across and two units in height (the dotted region in Fig. 14), we use an etch rate of

$$R = e^{-64(x-0.5)^2}(\cos^2(6y) + 0.01). \tag{38}$$

We start with a flat initial front and allow it to propagate downwards with etch rate given by the above. In the first column of Fig. 14, we show the results of mesh refinement of this etch rate using our first-order method narrow band method. As the grid is refined, the overshoot that occurs in the leading part of the propagating front diminishes until the correct solution is reached. Further refinement of the first-order narrow band method yields the same converged shape.

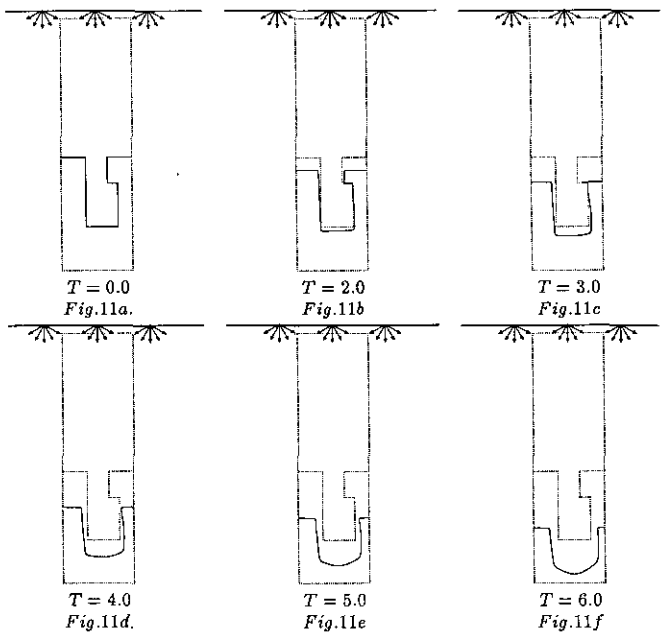

FIG. 11. Etching into cavity.

Next, we study the effects of using the full level set method and update all the level sets, not just those in the narrow band. We repeat the calculation using the full two-dimensional matrix technique in the second column of Fig. 14. The results on the coarsest grid is better for the full matrix than the narrow band approach because of the inaccuracy of the reinitialization on the coarse grid.

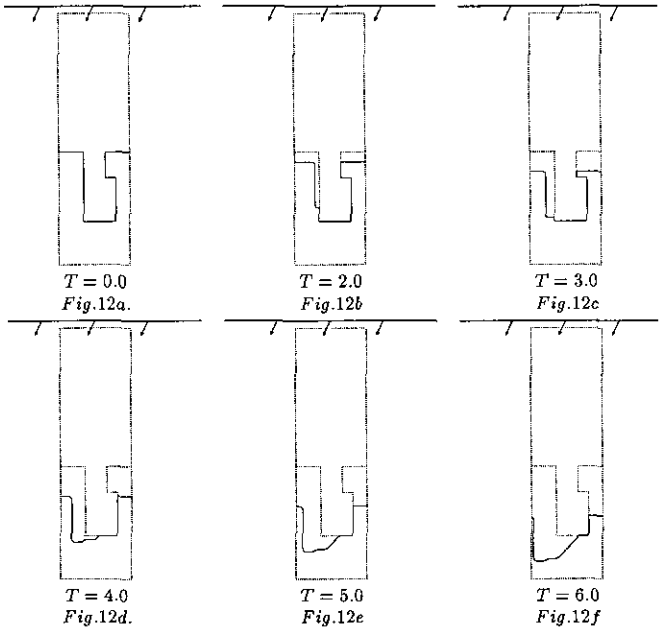

FIG. 12. Directional etching into cavity.

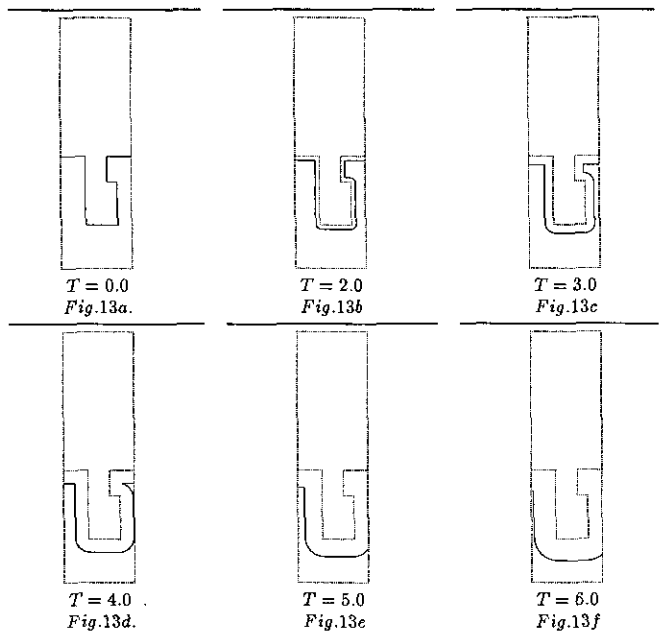

FIG. 13. Chemical etching into cavity.

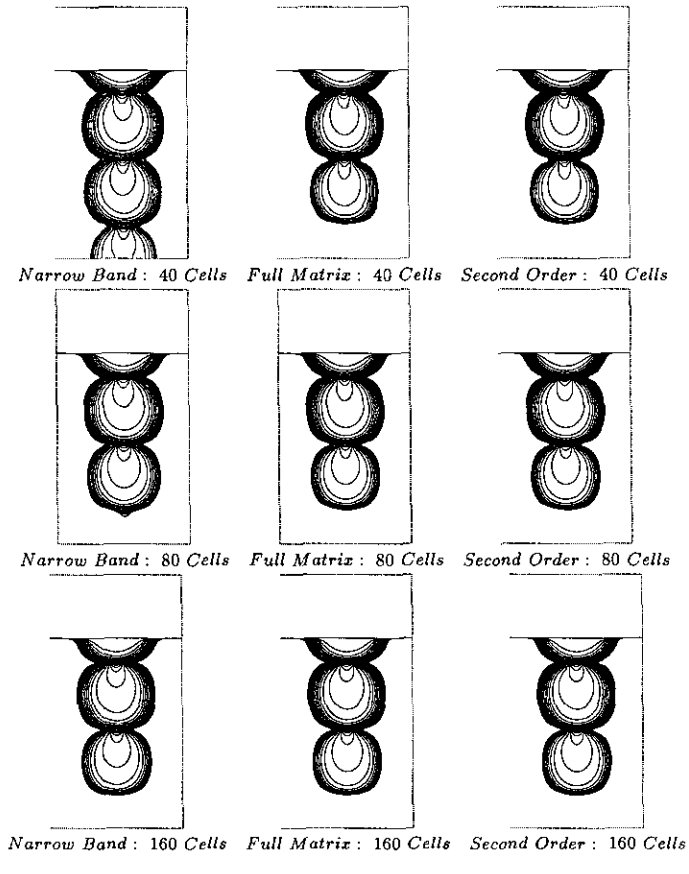

FIG. 14. Lithography under model gaussian

Finally, we analyze the effects of moving to a second-order in space narrow band scheme. In the last column of Fig. 14, we use a second-order operator split version of our scheme. Here, the second-order method achieves the converged shape on a coarse grid, as expected, verifying that high accuracy can be obtained in the front motion by using the technology of high resolution hyperbolic conservation laws. A second order in time method is possible using the predictor–corrector method outlined in [20]. In terms of timings, the narrow band calculation is around 10 times faster for the finest calculation than the full matrix solution.

In summary, similar to marker particle and cell methods, the narrow band approach requires work of order N to advance a front, where N is the number of cells in one dimension. Minimal extension is required off the zero level set, and high order schemes are readily available. The speedup resulting from the narrow band approach yields a highly competitive method.

6. SOME MODEL PROBLEMS

In this section, we perform some additional experiments to demonstrate the versatility of the level set approach.

6.1. Wet/Chemical Etching

We provide an example to demonstrate how the level set approach can follow complex changes in topology. We start with a square with masks covering segments of the boundary, and imagine the square surrounded by an etching substance. In Fig. 15, the etch eats into the non-masked walls, and the resulting front moves into the region and reconnects with other parts of the advancing front.

6.2. Sputter Etching/Deposition

In some problems (for example, ion milling), the normal speed of the profile depends on the angle of incidence between the surface normal and the incoming beam. This yield function is often empirically fit from experiment and has been observed to cause such effects as faceting at corners (see [15, 12]). To study this phenomenon, in Fig. 16 we consider several front motions and their effects on corners. We envision an etching beam coming down in the vertical direction. In all cases under study here, the angle θ shown in Fig. 5 refers to the angle between the surface normal and the positive vertical. For this set of calculations, in order to examine the geometry of sputter effects on shocks/rarefaction fan development, we ignore visibility effects. Following our usual notation, let $F(\theta)$ be the speed of the front in direction normal to the surface.

In column A we show the effects of purely isotropic motion, thus the yield function is $F = 1$. Located above the yield graph are the motions of an upwards and downwards square wave. In column B we show the effects of directional motion, thus

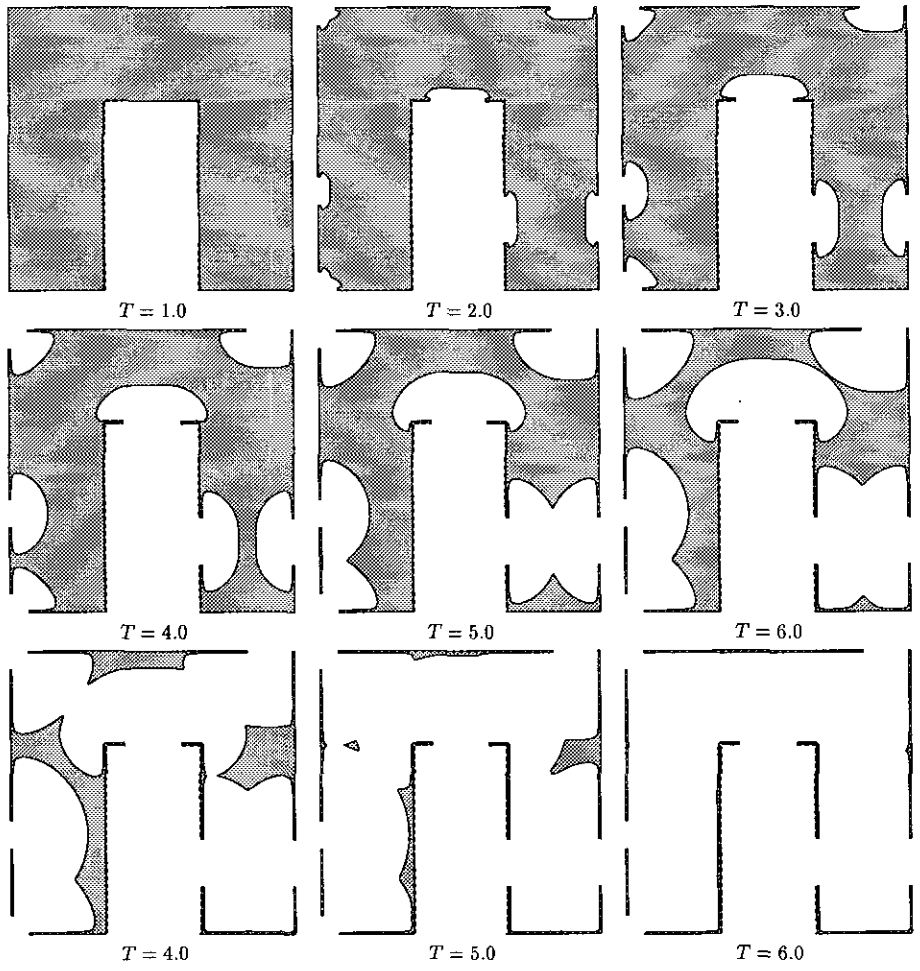

FIG. 15. Chemical etching into multiply masked region.

the yield function is $F = \cos(\theta)$. Thus, horizontal components on the profile do not move, and vertical components move with unit speed. In column C we show the effects of a yield function suggested by Leon [14] of the form $F = [1 + 4 \sin^2(\theta)] \cos(\theta)$.

The results of these calculations are shown in Fig. 16. The results show that the effects of angle-dependent yield functions are pronounced. In column A the isotropic rate produces smooth corners, correctly building the necessary rarefaction fans in outward corners and entropy satisfying shocks in inward corners as discussed and analyzed in [26, 27]. In column B, the directional rate causes the front to be essentially translated downwards, with some slight rounding of the corners. In column C, the yield function results in faceting of inward corners where shocks form and slight overhangs in the construction of rarefaction fans.

These overhangs in fact represent the *wrong* weak solution to the equations when sharp corners are present; most noticeably in the case of the construction of rarefaction fans. They in fact occur because the schemes used so far assume a convex Hamiltonian, when in fact the sputter function under consideration yields a non-convex Hamiltonian.[1]

In more detail, start with the level set formulation

$$\phi_t + F|\nabla\phi| = 0, \tag{39}$$

where ϕ is the level set function and F is the speed in the normal direction. We may rewrite this in the standard form of a Hamilton–Jacobi equation, namely

$$\phi_t + H(\phi_x, \phi_y) = 0, \tag{40}$$

where the Hamiltonian $H(\phi_x, \phi_y) = F(\phi_x^2 + \phi_y^2)^{1/2}$. When the speed function F does not depend on ϕ_x or ϕ_y, it is easy to check that the Hamiltonian H is convex. Thus, we can use the schemes presented earlier; they can be proved to produce the

[1] We thank O. Hald for his contributions to this analysis of a non-convex sputter law.

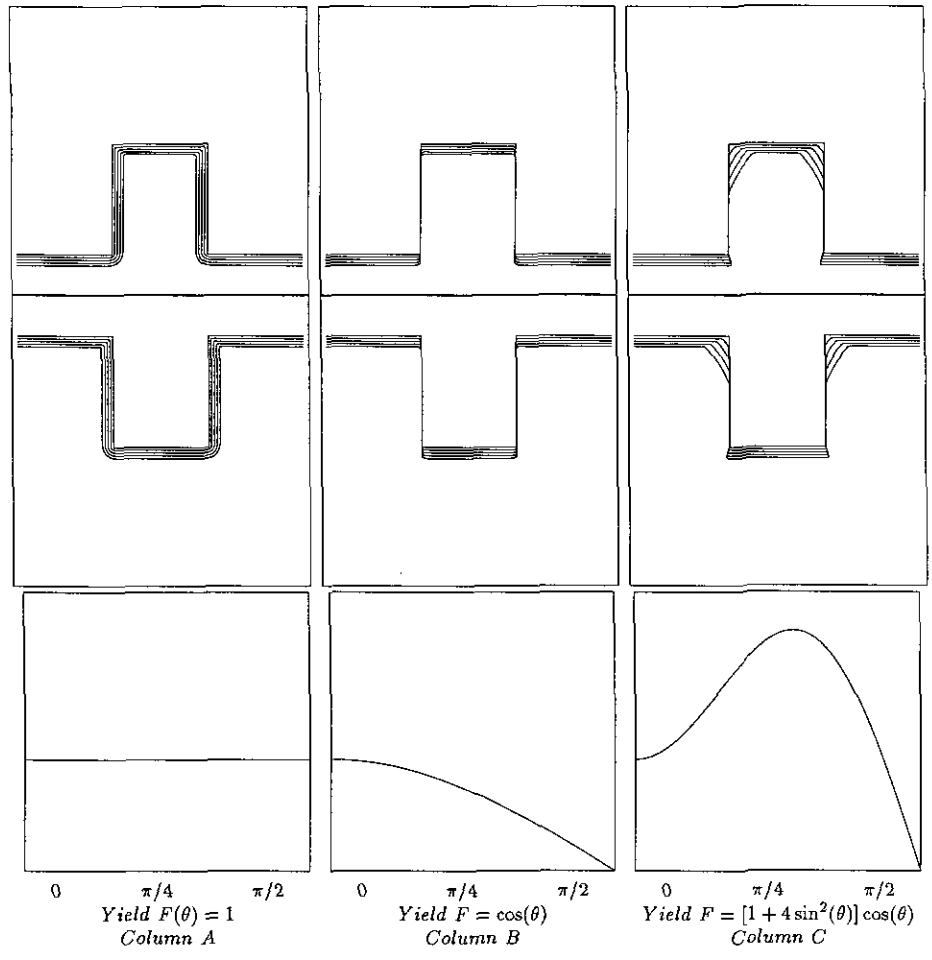

FIG. 16. Effect of different yield functions.

correct viscous solution which satisfies the appropriate entropy condition.

However, consider the case of the sputter function yield function given by the above, namely

$$F = (1 + A \sin^2(\theta)) \cos \theta, \tag{41}$$

where θ is the angle to the vertical. $A = 0$ produces no angle dependence, $A = 4$ produces a typical sputter case. We begin by writing this in the above form, namely

$$\phi_t + F|\nabla\phi| = \phi_t + [(1 + A)\cos\theta - A\cos^3\theta]|\nabla\phi|. \tag{42}$$

Noting that $\cos\theta = \phi_y/|\nabla\phi|$, some manipulation produces

$$\phi_t + H(\phi_x, \phi_y) = 0, \tag{43}$$

where the Hamiltonian H is now

$$H = (1 + A)\phi_y - A(\phi_y^3/|\nabla\phi|^2).$$

This Hamiltonian is in fact non-convex, and hence different difference schemes must be employed. We use a second order in space ENO version of Lax–Friedrichs (see [21]), given by

$$\phi_{ij}^{n+1} = \phi_{ij}^n - \Delta t\left[H\left(\frac{D_{ij}^{-x} + D_{ij}^{+x}}{2}, \frac{D_{ij}^{-y} + D_{ij}^{+y}}{2}\right) - \frac{1}{2}M_u(D_{ij}^{+x} - D_{ij}^{-x}) - \frac{1}{2}M_v(D_{ij}^{+y} - D_{ij}^{-y})\right], \tag{44}$$

where M_u (M_v) is a bound on the partial derivative of the Hamiltonian with respect to the first (second) argument.

This scheme can be proved to produce the correct viscous entropy-satisfying solution. When we use this scheme as in the below calculations given Fig. 17, the corners are sharp in column B and the overhangs disappear in column C. As a final test, in Fig. 18, we compare results with those obtained by the method of characteristics solution (see, for example, [15, 12]), showing excellent agreement.

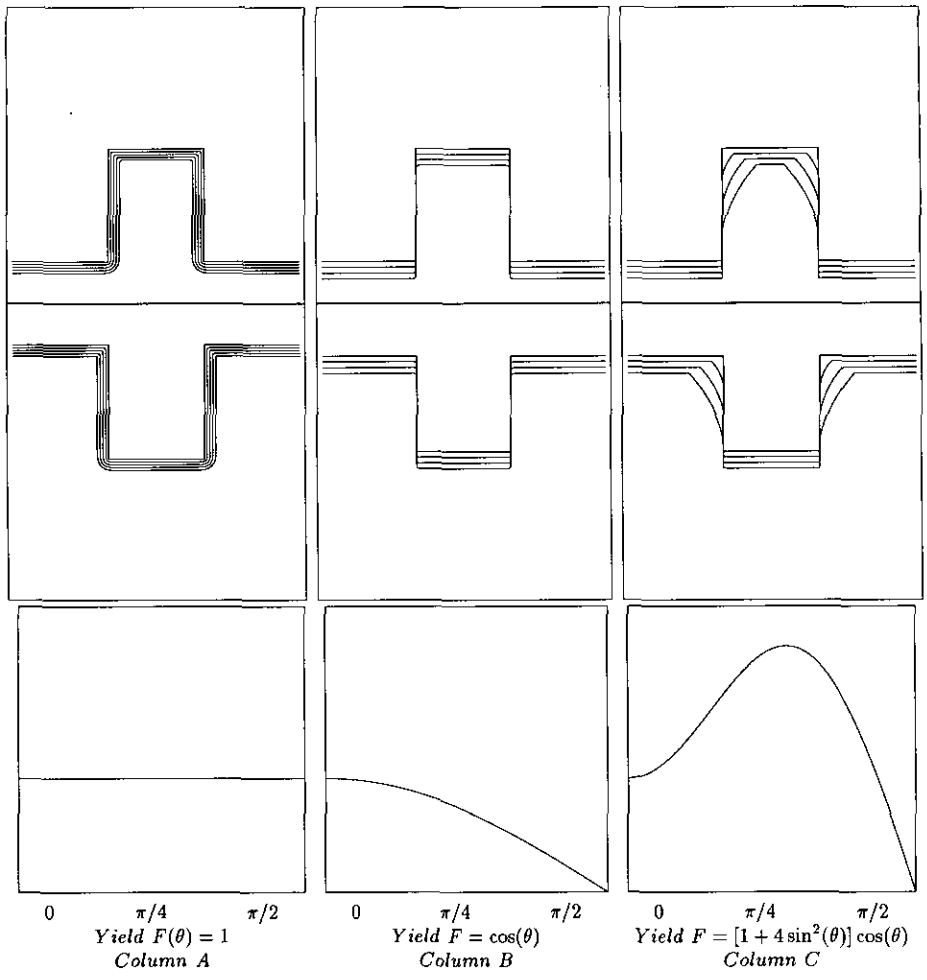

FIG. 17. Effect of different yield functions: Non-convex scheme.

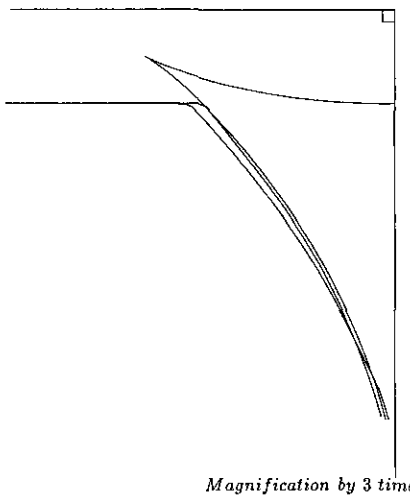

FIG. 18. Comparison with method of characteristics.

6.3. Multiple Materials/Discontinuous Etch Rates

Next, we study the effects of etching through different materials. In this example, the etch rates are discontinuous, and hence sharp corners develop in the propagating profile. The results of these calculations are shown in Fig. 19. A top material masks a lower material, and the profile etches through the lower material first and underneath the upper material. The profile depends on the ratio of the etch rates. In Fig. 19a, the two materials have the same etch rate, and hence the front simply propagates in its normal direction with unit speed, regardless of which material it is passing through. In Fig. 19b, the bottom material etches four times faster than the top; hence some degree of penetration underneath the top material occurs. In Fig. 19c, the ratio is ten to one, and finally, in Figure 19d, the ratio is forty to one, in which case the top material almost acts like a mask.

We next demonstrate the power of the method by considering etching through multiple materials. In Fig. 20, we show an etching front moving through blocks of materials with differing

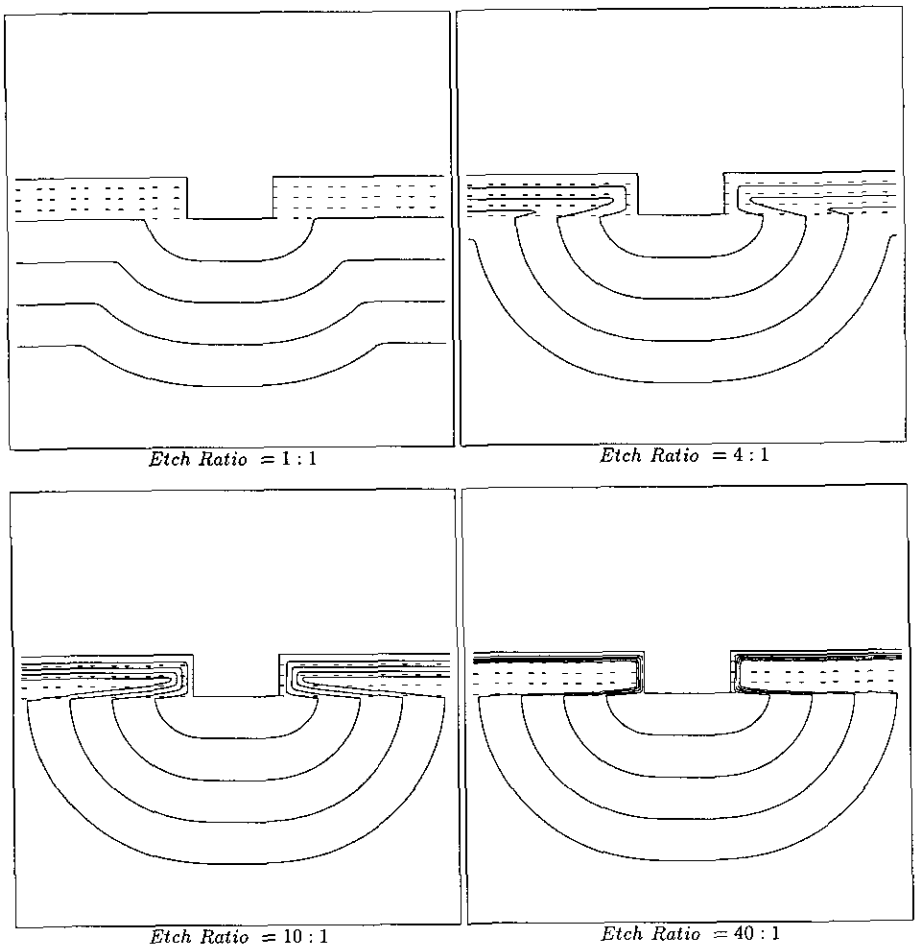

FIG. 19. Etch ratio = Bottom material rate to top material rate.

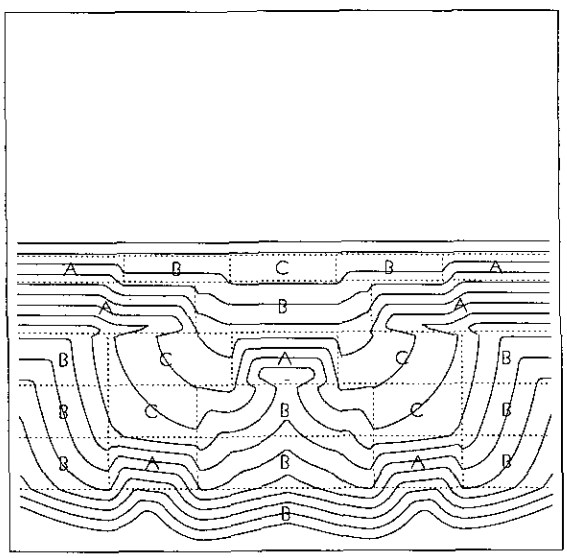

FIG. 20. Etching of multiple materials: Etch rates: A = 0.25, B = 0.5, C = 1.0.

etch rates. The results show the ability of the method to follow sharp variations in etch rate from material to material.

7. FUTURE WORK

The numerical method presented in this paper can be used for a wide variety of two-dimensional simulations in etching, deposition, and lithography; the method naturally takes into account such effects as incident angles, masks, yield functions, visibility, and anisotropy on the surface motion. Due to the use of conservative upwind schemes, the method selects the correct entropy condition and maintains sharp corners where shocks in the tangent occurs; conversely, the correct rarefaction fan solution is built at outward-facing corners. The method is second-order accurate in the motion of the front. By using the narrow band approach, the method is roughly 10 times faster for a reasonably sized problem than the full matrix method and is of the same computational work as cell and marker particle methods; that is, the work is a constant times the number of points which characterize the evolving front.

The extension of this work to three dimensions is straightfor-

ward and will be presented in part II of this paper (see [2]). Further work will include surface diffusion effects and reflection/re-emission issues.

ACKNOWLEDGMENTS

A video tape of the simulations shown here is available on request. All calculations were performed at the University of California at Berkeley and the Lawrence Berkeley Laboratory. We thank B. Coughran, J. Helmsen, O. Hald, P. Leon, A. Neureuther, C. Rafferty, J. Rey, V. Singh, K. Smith, and K. Toh for helpful discussions.

REFERENCES

1. D. Adalsteinsson and J. A. Sethian, *J. Comput. Phys.* **118** (1995).
2. D. Adalsteinsson and J. A. Sethian, *J. Comput. Phys.*, to appear.
3. A. Bourlioux and J. A. Sethian, in preparation.
4. Y. Chen, Y. Giga, and S. Goto, *J. Differential Geom.* **33,** 749 (1991).
5. Y. C. Chang, T. Y. Hou, B. Merriman, and S. J. Osher, *J. Comput. Phys.*, submitted.
6. D. L. Chopp, *Comput. Phys.* **106,** 77 (1993).
7. D. L. Chopp and J. A. Sethian, *J. Exp. Math.* **2,** No. 4, 1993.
8. L. C. Evans and J. Spruck, *J. Differential Geom.* **33,** 635 (1991).
9. M. Grayson, *J. Differential Geom.* **26,** 285 (1987).
10. J. J. Helmsen, Ph.D. dissertation, EEC, University of California, Berkeley, 1994.
11. J. J. Helmsen and A. R. Neureuther, *3D Lithography Cases for Exploring Technology Solutions and Benchmarking Simulators*, SPIE, Vol. 1927, Optical/Laser Microlithography VI, p. 382, 1993.
12. I. V. Katardjiev, G. Carter, and M. J. Nobes, *J. Vac. Sci. Technol. A* **6**(4), 2443 (1988).
13. R. Kimmel and A. Bruckstein, Center for Intelligent Systems Report No. 9209, Technion-Israel Institute of Technology, June 1992.
14. F. A. Leon, personal communication, 1994.
15. F. A. Loen, S. Tazawa, K. Saito, A. Yoshi, and D. L. Scharfetter, *Numerical Algorithms for Precise Calculation of Surface Movement in 3-D Topography Simulation, 1993 International Workshop on VLSI Process and Device Modeling (1993 VPAD).*
16. R. Malladi, J. A. Sethian, and B. C. Vemuri, Center for Pure and Applied Mathematics, IEEE Transactions on Pattern Analysis and Machine Intelligence, Vol. 17, No. 2, 1995.
17. J. P. McVittie, J. C. Rey, A. J. Bariya, and others, "SPEEDIE: A Profile Simulator for Etching Deposition, in *Proceedings of the SPIE—The International Society for Optical Engineering, 1991*, Vol. 1392, p. 126.
18. J. P. McVittie, J. C. Rey, L. Y. Cheng, and M. M. IslamRaja, "LPCVD Profile Simulation Using a Re-emission Model," in *International Electron Devices Meeting 1990*, Technical Digest, New York (IEEE, New York, 1990), p. 917.
19. W. Mulder, S. J. Osher, and J. A. Sethian, *J. Comput. Phys.* **100,** 209 (1992).
20. S. Osher and J. A. Sethian, *J. Comput. Phys.* **79,** 12 (1988).
21. S. Osher and C. Shu, *J. Comput. Phys.* **28,** 907 (1991).
22. J. C. Rey, L. Y. Cheng, J. P. McVittie, and K. C. Saraswat, *J. Vac. Sci. Technol. A* **9**(3), 1083 (1991).
23. C. Rhee, L. Talbot, and J. A. Sethian, J. Furip Mechanics, 1995 to appear.
24. E. W. Scheckler, Ph.D. dissertation, EECS, University of California, Berkeley, 1991.
25. E. W. Scheckler, K. K. H. Toh, D. M. Hoffstetter, and A. R. Neureuther, "3D Lithography, Etching and Deposition Simulation," in *Symposium on VLSI Technology, Oisio, Japan, 1991*, p. 97.
26. J. A. Sethian, Ph.D. dissertation, Dept. of Math., Mathematics, University of California, Berkeley, 1982.
27. J. A. Sethian, *Commun. Math. Phys.* **101,** p. 487 (1985).
28. J. A. Sethian, *J. Differential Geom.* **31,** 131 (1990).
29. J. A. Sethian, "Numerical Methods for Propagating Fronts," in *Variational Methods for Free Surface Interfaces*, edited by P. Concus and R. Finn (Springer-Verlag, New York, 1987).
30. J. A. Sethian, *J. Comput. Phys.* **115,** 1994.
31. J. A. Sethian, work in progress.
32. J. A. Sethian, submitted.
33. J. A. Sethian and J. D. Strain, *J. Comput. Phys.* **98,** 231 (1992).
34. V. K. Singh, S. G. Shaqfeh, and J. P. McVittie, *J. Vac. Sci. Technol. B.* **10**(3), 1091 (1993).
35. K. K. H. Toh, Ph.D. dissertation, EECS, University of California, Berkeley, 1990.
36. K. K. H. Toh and A. R. Neureuther, "Three-Dimensional Simulation of Optical Lithography," in *Proceedings SPIE, Optical/Laser Microlithography IV, 1991*, Vol. 1463, p. 356.
37. M. S. Young, D. Lee, R. Lee, and A. R. Neureuther, "Extension of the Hopkins Theory of Partially Coherent Imaging to Include Thin-Film Interference Effects," in *SPIE Optical/Laser Microlithography VI, 1993*, Vol. 1927, p. 452.
38. J. Zhu and J. A. Sethian, *J. Comput. Phys.* **102,** 128 (1992).